PHILOSOPHICAL TRANSACTIONS OF THE ROYAL SOCIETY A MATHEMATICAL, PHYSICAL & ENGINEERING SCIENCES

Harmonic wavelets in vibrations and acoustics

David E. Newland

Phil. Trans. R. Soc. Lond. A 1999 **357**, 2607-2625
doi: 10.1098/rsta.1999.0451

THE ROYAL SOCIETY

Harmonic wavelets in vibrations and acoustics

By David E. Newland

Department of Engineering, University of Cambridge, Trumpington Street, Cambridge CB2 1PZ, UK (den@eng.cam.ac.uk)

Four practical examples from mechanical engineering illustrate how wavelet theory has improved procedures for the spectral analysis of transient signals. New wavelet-based algorithms generate better time–frequency maps, which trace how the spectral content of a signal changes with time. The methods are applicable to multi-channel data, and time-varying cross-spectra can be computed efficiently.

Keywords: wavelet; harmonic; transient; time–frequency; cross-spectrum

1. Introduction

The author is interested in measuring and characterizing the dynamical behaviour of materials and structures. New techniques for the interpretation of transient and intermittent data, using wavelets, allow system and excitation properties to be deduced from measured data with more precision and greater speed than before.

The applications described in this paper come from the field of mechanical engineering. Four examples will be considered, three giving results that have not been published before. They involve the analysis of transient vibration signals. The practical objective is to extract as much information as possible from measured results. The signals may be short in duration because the phenomenon they represent happens quickly. Or their characteristics may change with time because of changes in the signals' underlying physical cause.

One example is the analysis of vibration data recorded during the transmission of bending waves in a beam subjected to impact loading. This is an essentially intermittent phenomenon as wave reflections occur and energy is transmitted backwards and forwards along the beam. Another similar, but more complicated, example uses data for pressure fluctuations recorded in an acoustic waveguide. Here there are many different waves interfering with each other. A third example uses data for ground vibration recorded near an underground train in London. Disturbance from the rumble of underground trains is becoming increasingly intrusive but it is very hard to predict. Finally, the fourth example computes time-varying cross-spectra for multi-channel measurements of soil vibration in a centrifuge test designed to model earthquake response. Simultaneously measured acceleration signals at different points allow the changing soil properties that occur under dynamic loading to be explored. The first two examples are laboratory demonstrations used as student experiments in the author's department. The second two examples are taken from research in progress at Cambridge for which wavelet analysis now provides an investigative tool of considerable importance.

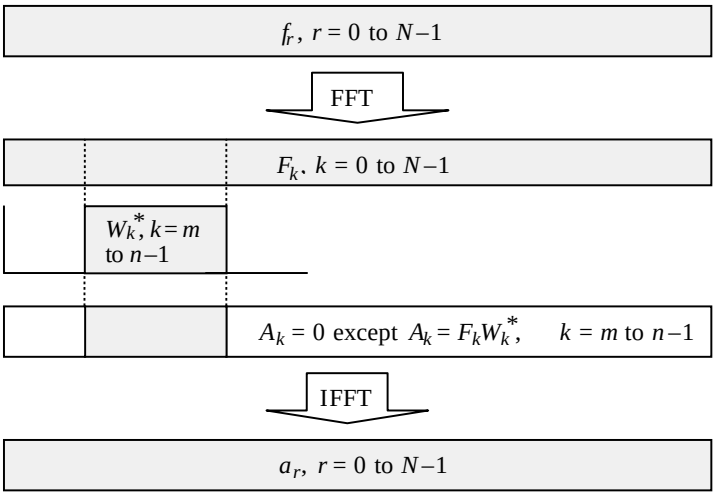

Figure 1. FFT algorithm to compute harmonic wavelet coefficients for wavelets in the frequency band $m2\pi \leqslant \omega < n2\pi$ (for a record of unit length).

2. Harmonic wavelet theory

The theory of harmonic wavelets has been described in previous papers by the author (Newland 1993, 1994*a*, *b*, 1998, 1999). In their simplest form, orthogonal harmonic wavelets provide a complete set of complex exponential functions whose spectrum is confined to adjacent (non-overlapping) bands of frequency. Their real part is an even function which is identical with the Shannon wavelet. Their imaginary part is a similar but odd function. Their equal spacing along the time axis is twice that of the corresponding set of Shannon wavelets. In their practical application, the box-car spectrum of harmonic wavelets is smoothed (to improve localization in the time domain) and the spectra of adjacent wavelet levels are overlapped to give oversampling in order to improve time–frequency map definition.

These wavelets have been found to be particularly suitable for vibration and acoustic analysis because their harmonic structure is similar to naturally occurring signal structures and therefore they correlate well with experimental signals. They can also be computed by a numerically efficient algorithm based on the fast Fourier transform (FFT).

For time–frequency mapping, there are similarities between the harmonic wavelet transform (HWT) and the short-time Fourier transform (STFT). The advantage of the HWT over the STFT is that the HWT is a computationally efficient variable-bandwidth transform. Therefore, the time–frequency map it generates can have a variable-bandwidth basis, with the analysing wavelet's bandwidth altered from one frequency to another to suit the problem being studied. In contrast, a time–frequency map constructed by the STFT always has a constant-bandwidth basis, giving the same frequency resolution at high frequencies as it gives at low frequencies. This means that the STFT is less flexible and may lead to a requirement for (much) more computation than is required by the harmonic wavelet transform. A detailed discussion of the merits of the two related methods is given in Newland (1998).

3. Numerical algorithm

A practical algorithm for time–frequency analysis is illustrated diagrammatically in figure 1 (Newland 1998). The correlation calculation at the heart of the wavelet method is carried out in the frequency domain, where it becomes a multiplication operation rather than a convolution. The input signal $f(t)$ is represented by the N-term series $f_0, f_1, f_2, \ldots, f_{N-1}$ in the top box. It is transformed from time to frequency by the FFT to give the Fourier coefficients $F_0, F_1, F_2, \ldots, F_{N-1}$ in the second box. The record length is assumed to be unit time, so that the sampling interval is $1/N$ and the Nyquist frequency $N\pi$. By definition, the (complex) harmonic wavelet has a Fourier transform W_k, $k = m$ to $n-1$, which is zero everywhere except in the range

$$m2\pi \leqslant \omega < n2\pi, \tag{3.1}$$

where $m < n$ (Newland 1994*b*). Because the wavelets are complex, their Fourier transform is one-sided, so that W_k remains zero for all negative frequencies.

On carrying out the multiplication operation, the F_k and W_k terms are multiplied to generate the new series

$$A_k = F_k W_k^*, \qquad k = 0 \quad \text{to} \quad N-1, \tag{3.2}$$

in the next box in figure 1. These A_k are the Fourier transforms of the wavelet coefficients. Computing their inverse (IFFT) reverts to the time domain to give the series of wavelet coefficients a_r, $r = 0$ to $N-1$, which are shown in the bottom box.

The time-scale runs from $0 \leqslant t < 1$ and $a_r = a(t = r/N)$ gives the result of calculating the wavelet coefficient for the wavelet centred at the chosen position $t = r/N$ on the time axis. The usual circularity property of the discrete Fourier transform method applies and when a wavelet runs off the end of the unit time-scale, it wraps round and reappears at the opposite end.

The computation in figure 1 therefore gives N wavelet coefficients for reference wavelets in all the possible N positions along the time axis. Only $n-m$ of these are needed to form an orthogonal set (Newland 1994*b*), and usually less than the (large) number N is needed to produce adequate resolution along the time axis. This is achieved by selecting $N1$ equally spaced values from the total available. If $N1$ is not a factor of N, appropriate methods of interpolation can be used. An efficient method of doing this is very important. The method used here is described in Newland (1999).

Instead of computing the IFFT of the N-term series A_k, $k = 0$ to $N-1$, in the lowest but one box in figure 1, this interpolation method computes the IFFT of a shorter $N1$-term series B_k, $k = 0$ to $N1-1$, whose first $n-m$ terms are the non-zero A_k, $k = m$ to $n-1$, and whose remaining terms are all zeros. It is shown in the reference that this generates a set of coefficients b_s, $s = 0$ to $N1-1$ that correspond to selected terms in the longer series a_r, $r = 0$ to $N-1$, provided that $sN/N1$ is an integer. If it is not, then the b_s interpolate between the nearest two values of a_r. The magnitudes of corresponding terms are the same. Therefore, a time–frequency amplitude map drawn by computing the shortened $N1$-term series b_s defined above will faithfully represent an amplitude map computed from the full-length N-term series a_r. The phase angles of corresponding terms will generally be

different according to (Newland 1999)

$$b_s = \exp(-\mathrm{i}2\pi ms/N1)a_{r=sN/N1}, \qquad s = 0 \quad \text{to} \quad N1 - 1, \tag{3.3}$$

but allowance can be made for these differences.

The centre frequency of the wavelet Fourier transform in figure 1 is $(m+n)\pi$ and its bandwidth is $(n-m)2\pi$. By changing the centre frequency, or bandwidth, or both, and repeating the calculation, a new series of wavelet coefficients, a_j, $j = 0$ to $N-1$, is generated. If this process is carried out for $N4$ different centre frequencies and each output series a_j downsampled to give $N1$ terms, the resulting $N4 \times N1$ array $A(N4, N1)$ is generated. This array is used to draw time–frequency maps to show how the amplitude and phase of the wavelet coefficients change over time and frequency. In the author's programs using these principles, the parameters $N1$ and $N4$ have the above meaning. Wavelet bandwidth is allowed to change linearly from $n - m = N2$ to $n - m = N3$ over the full frequency range of the calculation.

The algorithm in figure 1 applies for all harmonic wavelets, namely wavelets defined in the frequency domain with a compact spectrum such that $W(\omega) = 0$ outside a defined (generally narrow) band of frequencies. This no longer defines an orthogonal family of wavelets, but since reconstruction of the signal being analysed is not required, that does not matter. For the results given below, the boxcar spectrum of orthogonal harmonic wavelets has been windowed by a Hanning function, so that the function in the third box in figure 1 is given by

$$W_k = \frac{1}{2\pi(n-m)}\left(1 - \cos\frac{2\pi(k-m)}{n-m}\right), \qquad m \leqslant k < n. \tag{3.4}$$

This has been found to give good localization in the time domain.

4. Phase interpretation

This calculation procedure generates complex wavelet coefficients, a_r (figure 1). Their phase depends on the relative position of the signal and its analysing wavelet. This defines the ratio of the imaginary part of a_r (correlation with the odd part of the harmonic wavelet) to that of the real part of a_r (correlation with the even harmonic wavelet). When, for a constant harmonic signal, the wavelet is moved to a new position, its phase will be different. Therefore, absolute phase is not a useful indicator because it depends on wavelet location. But phase gradient, defined as the rate of change of phase with time for wavelets in the same frequency band, is an interesting parameter because it is constant when $f(t)$ is a harmonic of fixed frequency and phase. It is shown in Newland (1999) that, for a single harmonic of frequency ω_0, the phase gradient

$$\frac{\partial\phi}{\partial t} = \omega_0 - \Omega + \pi B, \qquad \Omega - \pi B \leqslant \omega_0 < \Omega + \pi B, \tag{4.1}$$

where Ω is the centre frequency and $2\pi B$ the bandwidth of the analysing wavelets.

The essential property is that the rate of change of phase with time is constant for a harmonic of fixed frequency and phase so that a two-dimensional map of phase gradient, with $\partial\phi/\partial t$ on a frequency–time base, is sensitive to phase changes in the signal being analysed. This will be illustrated in one of the examples of wave propagation given below, for which sudden changes in phase gradient occur in between successive reflections of energy in local frequency bands.

A different example in which absolute phase can be used helpfully is the last example in § 11, which is the analysis of simultaneous multi-channel recordings of ground movement after shock loading. Corresponding time records are analysed by the same wavelet arrays, with the wavelets in the same time location for the different channels. This enables differences in the phase of the channels to be detected and mapped as a function of time and position. It will be shown how changes in system properties (caused, for example, by soil slippage) can be detected by harmonic wavelet analysis from corresponding changes in the measured phase response.

5. Bending wave transmission in a beam

The first example comes from a laboratory experiment in the Department of Engineering at the University of Cambridge. The experiment illustrates bending wave propagation in a thin steel beam. The beam is suspended on light cords with its long axis vertical and is hit gently at one end by a soft-ended impulse hammer. This generates lateral bending waves which travel to the other (far) end of the beam, where they are reflected and return to the point of impact, before undergoing successive reflections until eventually they are dissipated by damping after several seconds. A small accelerometer is mounted on the beam so as to detect lateral vibration. For the results shown below, the accelerometer is positioned close to the first end of the beam, near its point of impact. The beam is 7.2 m long and has a rectangular cross-section $32.1 \times 6.3\,\mathrm{mm}^2$. The impulse hammer had a soft tip designed so that only low-frequency vibrations were generated (up to *ca.* 1 kHz). The sampling frequency was 4096 Hz.

Because the group velocity of bending waves depends on frequency (velocity proportional to frequency$^{1/2}$), groups of high frequency waves travel faster than low-frequency waves. Therefore a time–frequency map should show more frequent reflections for high frequencies than for low frequencies. This behaviour is, of course, not at all evident from the recorded time-domain response, which is shown for one second duration in the top view in figure 2, or from the spectrum which is drawn at the left-hand side of figure 2 with the frequency scale running from 0 to 750 Hz, approximately. A short length of this signal has been included in Newland (1998), but the full record has not been considered previously.

The map in figure 2 is a contour map of the three-dimensional surface obtained by plotting the magnitude of the wavelet coefficients against time and frequency. To plot the diagram, the bandwidth of the harmonic wavelets has to be chosen and, in the example given, bandwidth is changed in proportion to centre frequency. That chosen is indicated on the map by the small rectangular 'tile' in the top and bottom right corners. The height of this tile shows the bandwidth B Hz of the analysing wavelet at that frequency; the width of the tile shows the (mean-square) width of the wavelet T s, satisfying the uncertainty limit $BT = 1$.

As time passes, the regular pattern of curved ridges in figure 2 is interrupted by some transverse 'valleys' that run from left to right in the figure. These appear to be caused by non-bending modes into which vibrational energy 'leaks' as the wave propagation process continues. Within the frequency range of figure 2, there are about 50 bending modes which are excited. There are also about nine twisting modes and two longitudinal modes whose frequencies lie in range. Some of these may be unintentionally excited by the impulsive input being slightly away from the

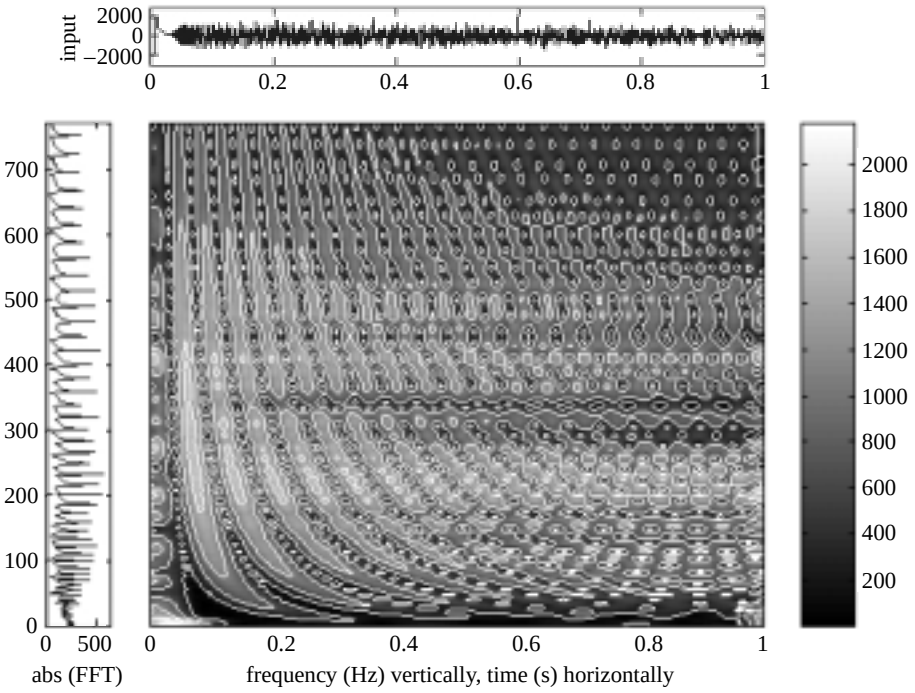

Figure 2. Amplitude time–frequency map for the bending vibration of a thin steel beam subjected to impact loading at one end. The acceleration response is measured close to the point of impact. Top view, time history; left, spectrum; right, density scale for wavelet amplitude (all arbitrary units).

geometrical centre of the beam or slightly off-line in direction, or they may be coupled to the bending modes, for example by the action of the supporting elastic cords or the mass loading of the accelerometer.

When a harmonic wavelet with a narrower bandwidth is used for the analysis, reduced definition along the time axis is achieved; for a harmonic wavelet with a wider bandwidth, reduced definition along the frequency axis is obtained (specific examples are given in Newland (1998)). The 'optimum' is determined by trial and error, guided by the shape of the uncertainty tile.

The unavoidable smearing of spectral features that occurs in figure 2 can be reduced by plotting only the ridges of the three-dimensional surface whose contours generate the figure. The exact identification of ridges is difficult (Eberly 1996) and identifying their precise position is complicated. The approach used by the author (Newland 1999) is to seek the height maxima of sections cut in the direction of the (smoothed) surface's greatest curvature. When this strategy is applied to the surface plotted in figure 2, the result is that shown in figure 3. Each ridge marks the arrival at the measurement point of successive groups of bending waves. At high frequencies the group velocity is higher, so successive reflections arrive more quickly than at low frequencies, when the ridges are further apart. Knowing the length of the beam, by measuring the time between successive reflections, the group velocity can be estimated as a function of frequency.

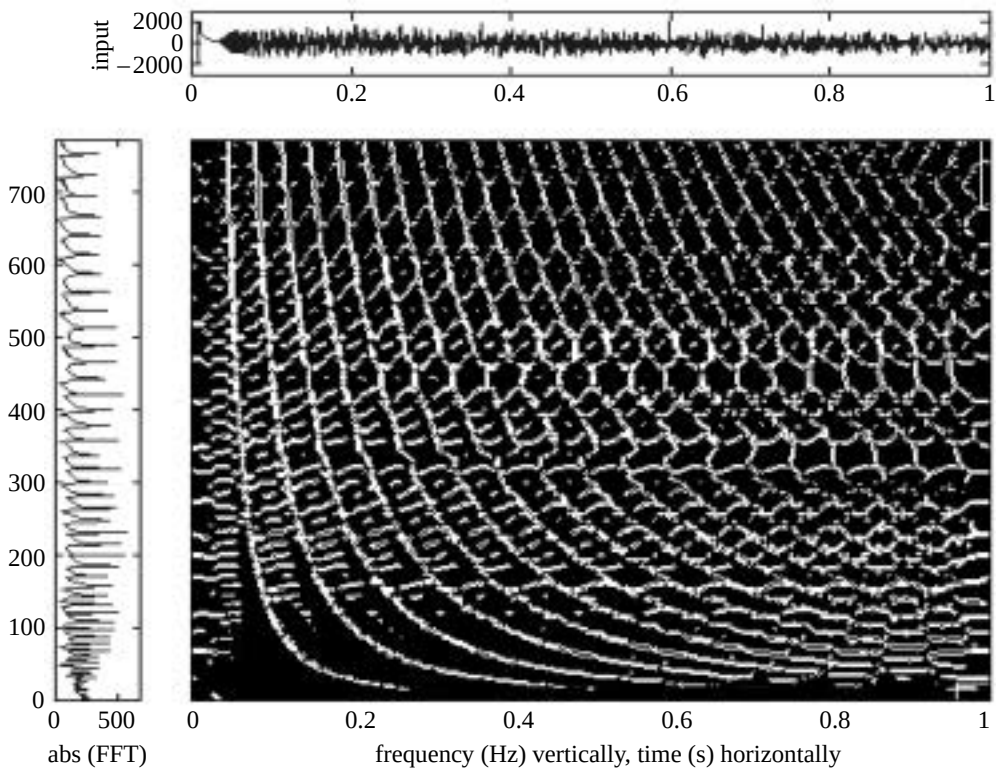

Figure 3. Ridges of the amplitude time–frequency map in figure 2.

6. Response of an acoustic waveguide

A similar, but more complicated, example is provided by the reflection of pressure waves within an acoustic waveguide. This is also a laboratory experiment at Cambridge. Internal air pressure perturbations are generated in a closed circular duct of approximately 12 m length and 0.75 m diameter. These perturbations are caused by a pulse-like electrical input to a small loudspeaker mounted near the edge of one of the rigid ends of the duct. This excites several different families of acoustic waves, which travel backwards and forwards within the duct. A microphone mounted at the centre of the end with the loudspeaker records the resulting pressure fluctuations and this signal has been used to generate the diagrams in figures 4 and 5.

Figure 4 shows the ridges of an amplitude time–frequency map, computed as described above. In addition to the main ridges, there are numerous small, generally horizontal ridges which arise from local fluctuations in surface height. They can be eliminated by introducing more smoothing before ridge detection and it is a matter of judgement to generate the ridge map which is the 'best' for a required purpose. As for figure 3, figure 4 has the input time history shown for comparison along the top, and the modulus of this signal's Fourier transform plotted along the left-hand side (using arbitrary units). For convenient scaling, the square root of the Fourier transform is plotted.

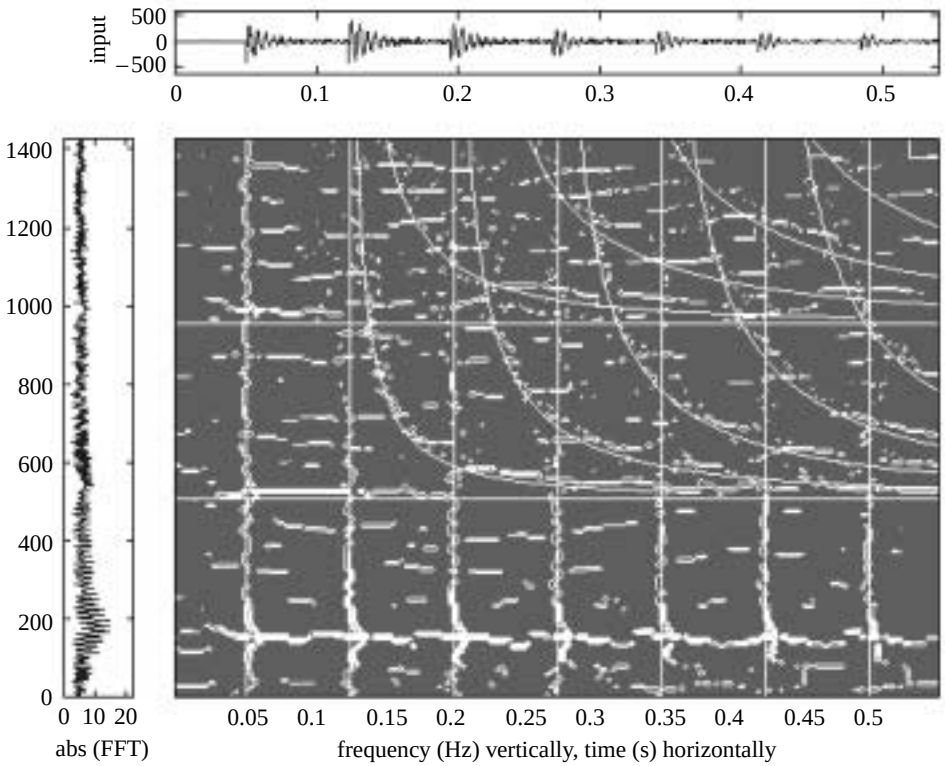

Figure 4. Time–frequency ridge map of acoustic reflections in a closed duct: comparison of theory and experiment (from Newland 1999).

The underlying physical processes represented in this map are quite complicated. Axial, plane waves travel at constant velocity (independent of frequency) and bursts of energy from these plane waves arrive periodically at the microphone. They show as equally spaced vertical lines in figure 4. Knowing the dimensions of the duct and the acoustic properties of air, the position of these lines can be calculated and their theoretical position is superimposed on their experimental position in figure 4. Within the frequency range of these maps there are two other families of non-axial waves which are dispersive (their group velocity depends on frequency). Their passage time between reflections is given by

$$T(\omega) = \frac{2L}{c\sqrt{1 - \Omega_0^2/\omega^2}}, \tag{6.1}$$

where $L = 12.16\,\mathrm{m}$ is the length of the duct, $c = 334\,\mathrm{m\,s^{-1}}$ is the speed of sound, ω is the wave frequency, and Ω_0 is the cut-off frequency. For plane waves, the cut-off frequency is zero, and for the first two families of non-axial waves which are detected by a microphone at the centre of the duct it is $\Omega_0 = 3.83c/a$ and $7.02c/a$, where $a = 0.386\,\mathrm{m}$ is the duct's radius (see, for example, Skudrzyk 1971, p. 431). These results have been used to plot the theoretical lines on figure 4, measuring time forward in steps of $T(\omega)$ from the instant of impulsive excitation.

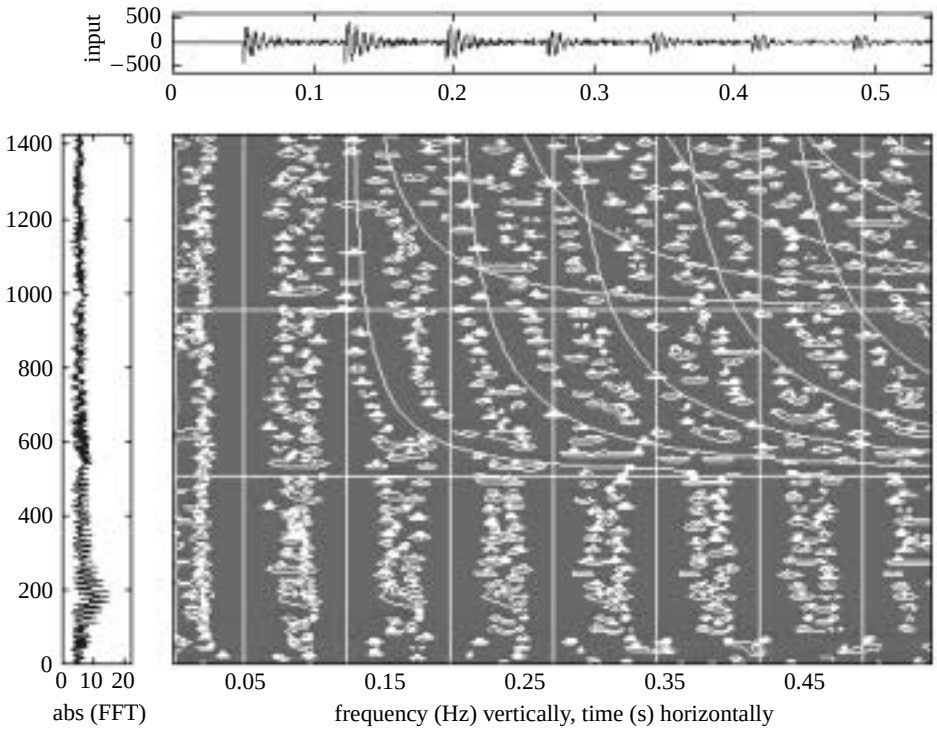

Figure 5. Time–frequency differential phase map corresponding to figure 4 (from Newland 1999).

The calculated cut-off frequencies are plotted as the horizontal lines in figure 4. Successive reflections of the dispersive waves appear as the two families of curved lines that are asymptotic to the cut-off lines. The horizontal ridge at *ca.* 200 Hz is due to ringing of the loudspeaker's diaphragm and is not associated with the travelling wave acoustic phenomena.

Figure 5 shows a differential phase map of the same data. It is a contour plot of the three-dimensional surface obtained by plotting the modulus of phase gradient on a base of frequency versus time. It can be seen that phase perturbations occur generally between ridge positions indicating phase changes at every reflection of the travelling wave energy. A characteristic of this presentation is that the vertical distribution (distribution over frequency) of the phase perturbations is correlated with the position of the peaks in the Fourier transform of the input signal (plotted along the left-hand side). By placing a straight edge across a similar diagram drawn to larger scale, it can be shown that the phase perturbations align quite closely with the positions of the troughs in the spectral data plotted on the left-hand side (Newland 1999). This is not evident so clearly in corresponding graphs of wavelet amplitude.

7. Underground train vibration

The transmission and attenuation of ground-borne vibration is an extremely difficult computational problem because of the geometric complexity of ground and building

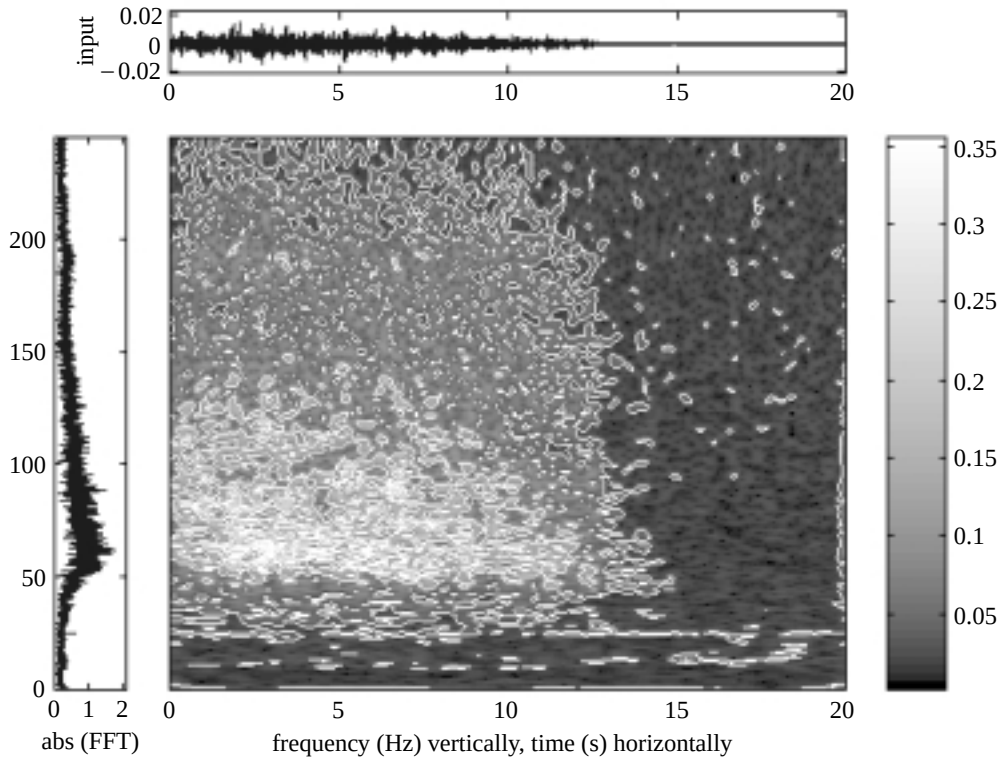

Figure 6. Time–frequency analysis of the recorded ground acceleration during the passage of a train on a nearby underground railway line.

structures and because of lack of understanding of the dynamic response properties of soils and foundations (Newland & Hunt 1991, 1992, 1996). For example, for the new Folkestone to London high-speed railway line, there are currently no agreed protocols to compute groundside vibration or the level of anticipated disturbance in local buildings, old or new. This is a serious, and currently unsolved, design problem.

Recently, ground acceleration data have been measured near to a curved section of the Piccadilly underground line in London. For the results given here, an accelerometer was secured to a stone step in an adjacent building and 20 s of the passage of a train recorded. The time history of this process is shown in the upper view in figure 6, the units being gs. The recording begins with the train already passing, and continues until it has passed out of hearing in 20 s.

Figure 6 shows a harmonic wavelet amplitude map for this vibration, covering the frequency range from 0 to 250 Hz (half the Nyquist frequency of 500 Hz). It is evident that there is a broadband response as the train passes, with ground vibrational energy in a wide range of frequencies as a result of wheel and rail surface irregularities, wheel flange-to-rail contact, mechanical train noise and electrical collector noise.

Examination of the higher-frequency content of the recorded signal for the first 5 s of the data (figure 7) shows a marked local variation in vibrational intensity. This is apparent from the mean-square graph plotted in figure 8 (bottom), which is the energy represented by the appropriate summation of wavelet amplitudes squared, for

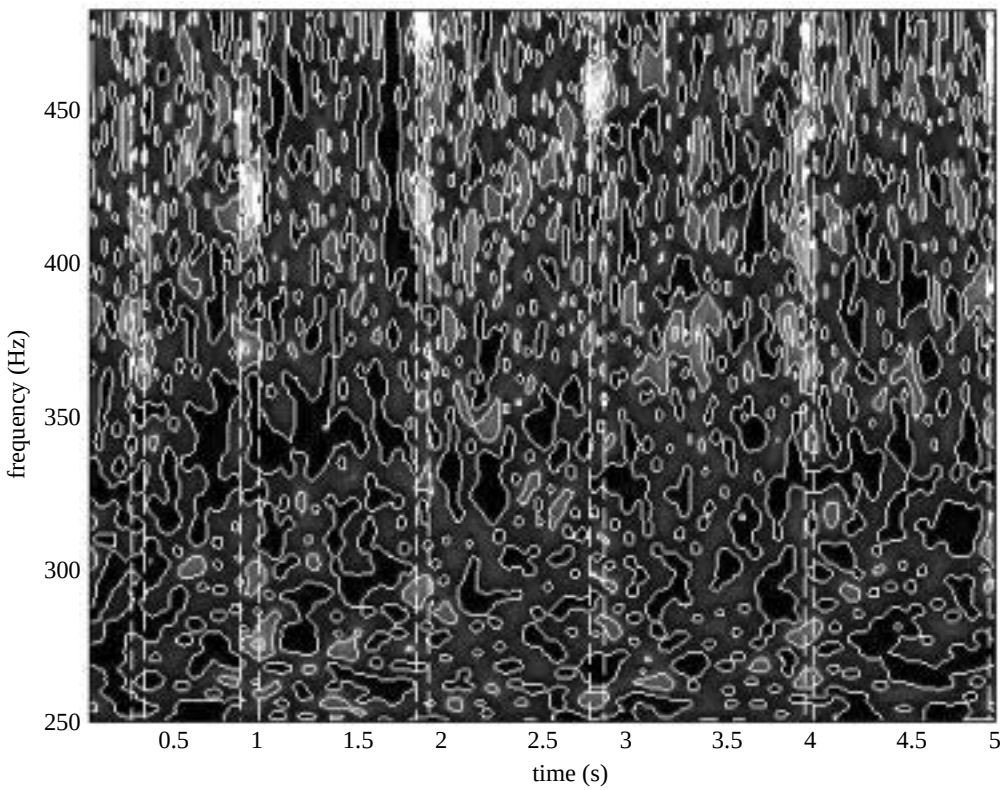

Figure 7. Analysis of part of the same data as in figure 6, with segmentation markers to identify locally high-amplitude response.

the frequency band of figure 7 (only). Above it in figure 8, the amplitude discriminator $d(j)$ is plotted, where $j = 1$ to 300 is the index of columns in figure 7. This function is a measure of the amplitude difference of all the wavelet coefficients (in the frequency band considered) between one column of the array plotted in figure 7 and the immediately adjacent column (Tait & Findlay 1996; Newland 1998). The segmentation markers in figures 7 and 8 are chosen to coincide with local peaks in $d(j)$ and provide a means of identifying the extent of the mean-square peaks in the bottom view in figure 8. These local peaks of high-intensity vibration appear to result from intermittent impact between wheels and rails. It can be seen from the top view in figure 8 that there is a degree of arbitrariness in the selection of the appropriate peaks of the amplitude discriminator $d(j)$ which denote a sudden change in vibrational spectral content. The likely explanation is that the onset and termination of the wheel flange to rail interaction process is variable and that the response to this process is confused by the vibration generated by other sources, in particular by rail joints and irregularities.

8. Geotechnical centrifuge testing

Fundamental knowledge of the (large amplitude) dynamic behaviour of soil under earthquake excitation is meagre. Studies at Cambridge in our Geotechnical Cen-

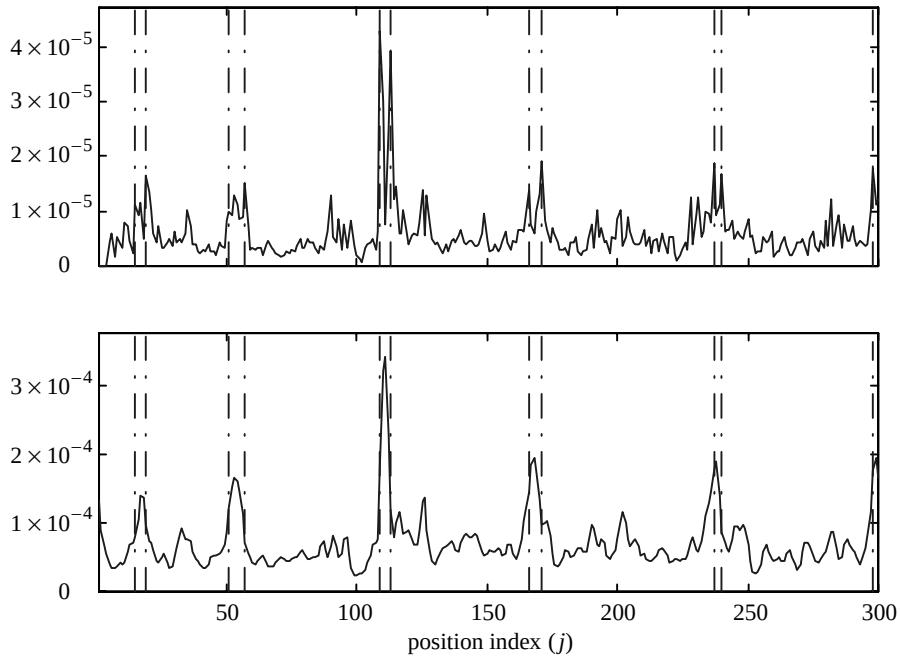

Figure 8. Bottom: mean-square response for the frequency band shown in figure 7. Top: amplitude discriminator $d(j) = \sum_k (|a(k,j)| - |a(k,j-1)|)^2$, where $a(k,j)$ is an element in the two-dimensional array plotted in figure 7. The index j runs from 1 to 300 because the map in figure 7 is plotted from an array which has 300 columns.

trifuge Centre and elsewhere (Lee & Schofield 1988; Taylor 1995; Butler 1999; and others) have obtained good data on the transient vibration of soil models under earthquake conditions. The levels of excitation cause large deflection intergranular movements which lead to so-called soil liquefaction effects when the soil's response is closer to that of a fluid than a solid. Because excitation lasts only for a second or two with excitation frequencies ranging up to *ca.* 200 Hz, data analysis can only be done if there are good methods of transient vibration analysis. Wavelet methods make this possible and good preliminary results have already been achieved using harmonic wavelets (Newland & Butler 1998). New research is concentrating on developing these methods to estimate time-varying cross-spectra between adjacent measuring points. This is seen as a very important area of further theoretical and experimental research.

9. Experimental data

The test data used below are those published in Newland & Butler (1998) and were obtained from geotechnical centrifuge tests. The experimental system represented a saturated sand model poured at two relative densities and mounted within a flexible container. The container is shown in figure 9. It is rectangular in shape with its side walls made of a series of flat rings, each mounted to the next by a rubber gasket. The intention is that the loaded container functions as an equivalent shear beam,

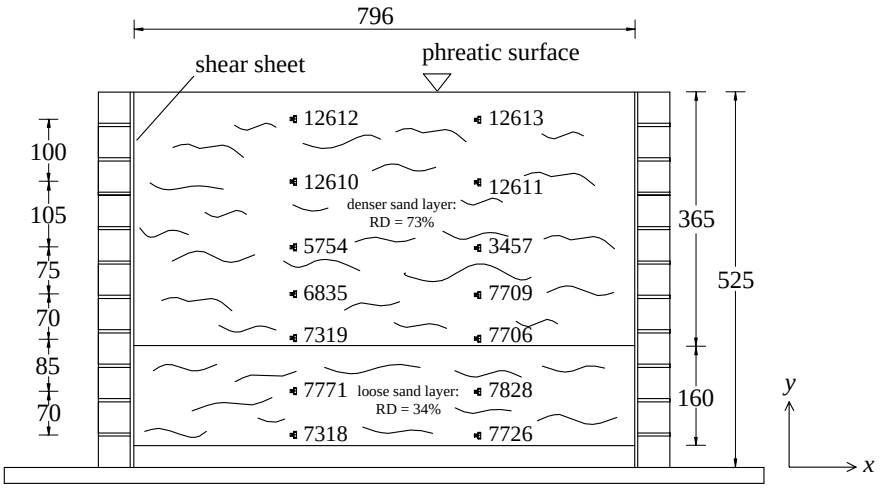

Figure 9. Instrumentation layout. All accelerometers have their sensitive axis in the x-direction (Newland & Butler 1998).

whose shear modulus matches approximately that of the enclosed soil medium. Sand was poured at a density of 1576 kg m^{-3} in the lower 160 mm of the container and at 1670 kg m^{-3} for the remaining 365 mm to the top of the container.

The container and its contents were centrifuged to apply an acceleration vertically downwards (in figure 9) of 50g in order to simulate the response of a large ground volume in a small model. Horizontal shear excitation to the base of the container was supplied by a device called a stored angular momentum actuator. This consists of a flywheel which is connected to a reciprocating rack by a clutch assembly. When the clutch is engaged, there is a sudden burst of oscillatory energy which shakes the container and its contents while this is being centrifuged.

Sand movement was detected by miniature piezoelectric accelerometers. As seen in figure 9, these were stacked vertically within the test specimen with four in the bottom layer of sand and ten in the top layer. Previous tests have shown that they have an accuracy of ±5% within the frequency range 20 Hz to 2 kHz. Their natural frequency when embedded in sand is estimated to be *ca.* 4 kHz compared with frequencies of interest up to *ca.* 400 Hz. Each transducer was carefully orientated in the sand to record the resulting horizontal motion (the x-direction in figure 9) within the saturated model.

Data were stored in a digital data-acquisition system developed in Cambridge as part of the centrifuge's instrumentation, from which they are retrieved for detailed computer analysis. The input motion to the base of the model container had a fundamental frequency of 27 Hz with a displacement amplitude of ±1.5 mm. The duration of the shaking excitation was set to 1.2 s.

For purely harmonic movement, these displacements correspond to a lateral acceleration amplitude of *ca.* 4.4g. However, loose-play and nonlinearities in the mechanism introduce a harmonic content to the excitation, as will be apparent from the measured results below. The measurement points are shown in figure 9. The signals f_1 to f_6 were recorded at the following six locations: f_1 at 7726, f_2 at 7828, f_3 at

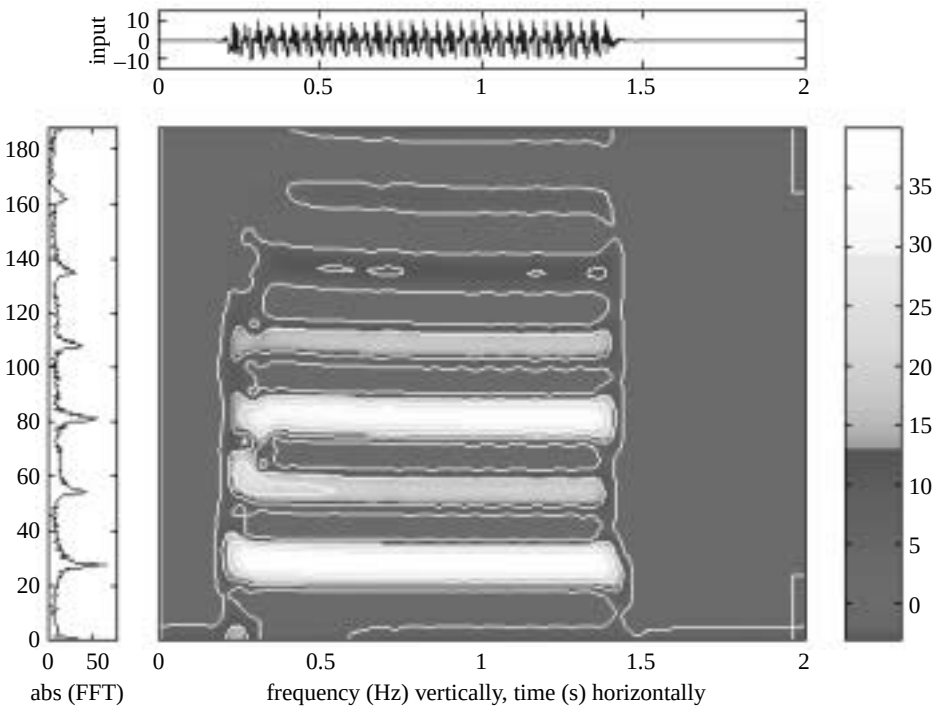

Figure 10. Experimental data: power spectral density for signal f_1 measured at position 7726 (see figure 9).

7319, f_4 at 7709, f_5 at 12 611 and f_6 at 12 612, but only two of these measurements, f_1 and f_4, are used for the results given below.

10. Power spectral densities

All signal processing computations have been done by the harmonic wavelet method using the algorithm described above. Results are shown as before as two-dimensional maps of three-dimensional surfaces plotted for the relevant parameter. For ease of identification for a multi-channel system, it is convenient to refer to (i) the power spectral density of a measurement, (ii) the amplitude of the cross-spectral density between two measurements, and (iii) the phase of the cross-spectral density. These terms are not strictly correct because they are defined for stationary random processes, whereas we are concerned with transient and non-stationary processes. However, the amplitude squared of the wavelet coefficient is called a power spectral density since, for an orthogonal set of harmonic wavelets, the mean-square signal is equal to the sum of the (weighted) wavelet amplitudes squared (see, for example, Newland 1993). When the signal is oversampled to generate extra wavelet coefficients, the same analogy may be used. Similarly, the product of two wavelet amplitudes, when computed for the same wavelet at the same instant of time for two signals, represents the amplitude of the cross-spectral density between these signals (for that time instant and frequency band). Also the phase difference between the same two wavelet coefficients gives the phase of the cross-spectral density between these signals.

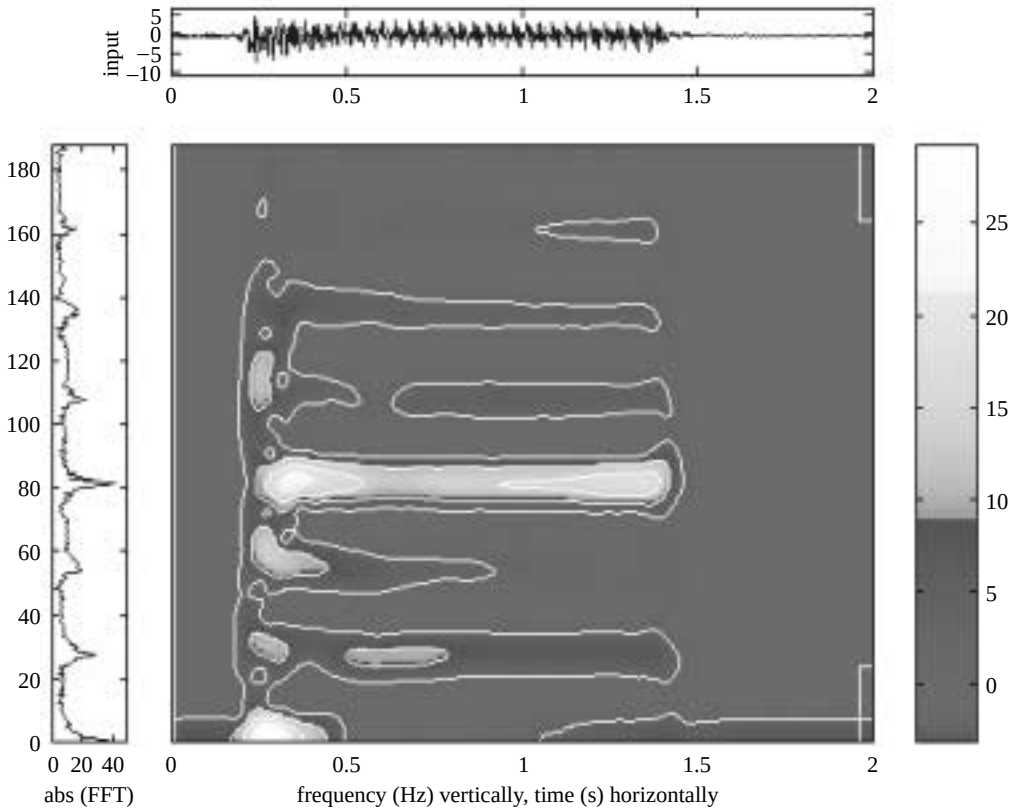

Figure 11. Experimental data: power spectral density for signal f_4 measured at position 7709 (see figure 9).

Time-varying auto-spectral densities calculated this way are plotted for records f_1 and f_4 (positions 7726 and 7709 in figure 9) in figures 10 and 11.

The forced displacement excitation of the base of the model consists of the fundamental component at *ca.* 27 Hz with unavoidable superimposed harmonics of all orders. These can be seen in figure 10. The time history f_1 is plotted along the top of the map and its power spectral density (also referred to as the auto-spectral density) is plotted along the left-hand side.

The amplitude map in figure 10 shows that the vibration close to the bottom of the box remains approximately constant as shaking continues because the horizontal stripes have approximately constant width and continue for the full duration of the shaking process. In contrast, all the other power spectral densities, for example f_4 in figure 11, show obvious changes with time. This must be due to the changing physical properties of the soil model as a result of its changing dynamic properties with time.

11. Cross-spectral densities

Power spectral density data indicate the total energy in a signal and its distribution over frequency and time. Relative changes in two signals are described by the cross-

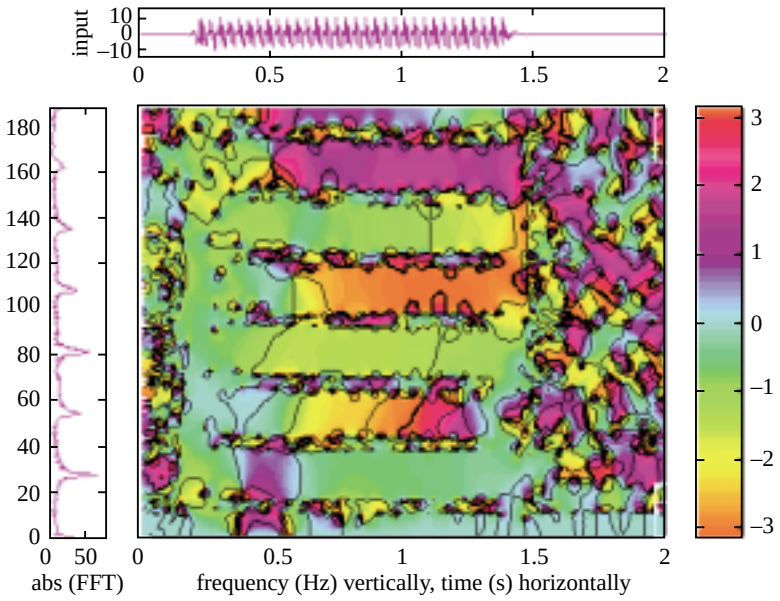

Figure 12. Experimental data: phase of cross-spectral density for signals f_4 and f_1 (measured at positions 7709 and 7726, see figure 9).

spectral density. This provides a measure of the local correlation between two signals. The cross-spectral density's amplitude is measured by the product of the wavelet amplitudes of both signals; its phase is measured by the wavelets' relative phase. As for all time–frequency analysis, all spectral calculations are estimates for the chosen frequency band and time window considered. For the harmonic wavelet method, this is defined by the bandwidth and time duration of the chosen wavelet, which is under the control of the investigator and is indicated by the shape of the rectangular 'tile' shown in the top right and lower right corners of the maps (vertical height equals the bandwidth, horizontal width equals the time duration).

For the experimental data, figure 12 shows the phase of the time-varying cross-spectral density for f_4 with f_1 These results have not been published before, and some explanation of their interpretation is needed. The density legend is shown on the right-hand side of figure 12. It runs from $\pi = 180°$ at one extreme to $-\pi = -180°$ at the other extreme. Before the forced motion has been applied, and after it has finished, there are residual noise signals and these give rise to the haphazard phase represented by 'marbling' on the right- and left-hand sides of the map. During the forced motion, the map has obvious horizontal stripes, each corresponding to one harmonic of the motion (identified on the left-hand side spectrum, which is for f_1). Around the fundamental frequency of 27 Hz, the density of the stripe indicates that f_4 and f_1 are approximately in phase with each other. The same is true for the second harmonic initially, but as motion continues there is a phase change from approximately zero through minus 90° and then through −180° to approach zero again. For higher harmonics, the density of each stripe changes as time passes, with the transition sometimes being quite sudden.

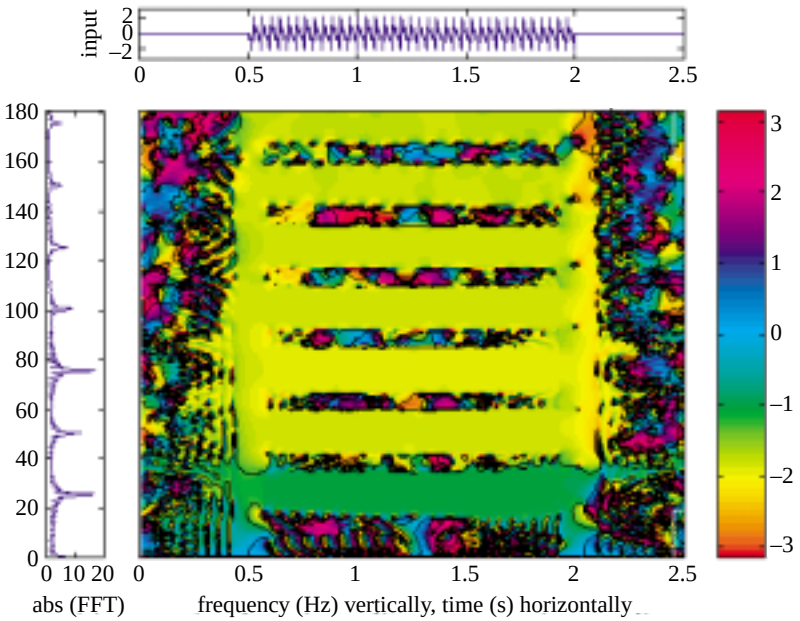

Figure 13. Simulated data: phase of cross-spectral density for signals f_2 and f_1 (at the middle and bottom of the model).

In between each horizontal stripe there is a thinner marbled stripe where there is uncorrelated response between two harmonics and phase coherence is not maintained.

12. Simulated results

For comparison with the experimental results, the behaviour of a linear model has been simulated. This model consists of a box in three horizontal sections (identified as 1:bottom, 2:middle and 3:top) with parameters chosen to give natural frequencies and damping ratios of 12 Hz, 0.13 and 31.5 Hz, 0.33. The fundamental frequency of the displacement excitation was set at 25 Hz and there are harmonics up to the 8th (200 Hz) included. The acceleration response of the model has been computed by numerically integrating the equations of motion (with the system's parameters constant). To model the experimental system, the deterministic response was supplemented by a low-amplitude random signal to represent noise.

Figure 13 is the phase of the cross-spectral density between f_2 and f_1 for the model (middle and bottom). The random noise causes the 'marbling' and the slight variations in colour density along each horizontal stripe. However, it can be seen from figure 13 that the cross-spectral phases remain approximately constant for each harmonic during the shaking phase.

By comparing figures 12 and 13, it is clear that significant phase changes occur during the duration of shaking in the experimental case (figure 12), which are not duplicated in the simulated comparison (figure 13).

By introducing time-varying parameters into a linear model, it is possible that the experimental results could be simulated. However gradual, progressive changes in parameters would not account for the observed behaviour. It is more likely that

nonlinear effects caused by sudden slippages, or liquefaction, or, as a result, abrupt contacts with the side walls of the model container may account for the observed behaviour. To properly simulate these effects is a challenging task!

The laboratory experiments which generated the beam bending and acoustic duct data were devised by my colleague Dr Jim Woodhouse. I am grateful to him for making the data available for analysis and for numerous discussions about the results. Dr Woodhouse and two of his colleagues first applied time–frequency analysis to similar problems some years ago, using the short-time Fourier transform method (Hodges *et al*. 1985). Dr Hugh Hunt has worked with me on problems of ground vibration transmission and I thank him for providing the measured underground train data included above. We hope that analysis of this and similar data will lead eventually to better means of alleviating traffic noise problems. The work of my colleague, Professor Andrew Schofield, who was responsible for the design and development of the Cambridge geotechnical centrifuge and its derivatives elsewhere in the world, is well known to foundation engineers (Schofield 1980; Schofield & Steedman 1988). I am grateful to Professor Schofield and his PhD student, Gary Butler, for providing the centrifuge data for which the wavelet analysis method has been able to illuminate transient dynamic behaviour in a way that had not previously been possible. Only some illustrative results are given above from the extensive data that are now being analysed by those working in this field.

References

Butler, G. D. 1999 A dynamic analysis of the stored energy angular momentum actuator used with the equivalent shear beam container. PhD thesis, Department of Engineering, University of Cambridge, UK.

Eberly, D. 1996 *Ridges in image and data analysis*. Englewood Cliffs, NJ: Prentice Hall.

Hodges, C. H., Power, J. & Woodhouse, J. 1985 The use of the sonogram in structural acoustics and an application to the vibrations of cylindrical shalls. *J. Sound Vib.* **101**, 203–218.

Lee, F. H. & Schofield, A. N. 1988 Centrifuge modelling of sand embankments and islands in earthquakes. *Geotechnique* **38**, 45–58.

Newland, D. E. 1993 Harmonic wavelet analysis. *Proc. R. Soc. Lond.* A **443**, 203–225.

Newland, D. E. 1994*a* Wavelet analysis of vibration. Part 1. Theory. Part II. Wavelet maps. *ASME J. Vib. Acoustics* **116**, 409–425.

Newland, D. E. 1994*b* Harmonic and musical wavelets. *Proc. R. Soc. Lond.* A **444**, 605–620.

Newland, D. E. 1998 Time–frequency and time-scale signal analysis by harmonic wavelets. In *Signal analysis and prediction* (ed. A. Procházka, J. Uhlír, P. J. W. Rayner & N. G. Kingsbury), ch. 1. Boston: Birkhäuser.

Newland, D. E. 1999 Ridge and phase identification in the frequency analysis of transient signals by harmonic wavelets. *ASME J. Vib. Acoustics* **121**, 149–155.

Newland, D. E. & Butler, G. D. 1998 Application of time–frequency analysis to strong motion data with damage. *Proc. 69th Shock and Vibration Symp., Session HB1, SAVIAC (Shock and Vibration Information Analysis Center, US Dept of Defense), Minneapolis.*

Newland, D. E. & Hunt, H. E. M. 1991 Isolation of buildings from ground vibration: a review of recent progress. *Proc. IMechE* C **205**, 39–52.

Newland, D. E. & Hunt, H. E. M. 1992 Isolating buildings from vibration. *Proc. 2nd. Int. Congress on Sound and Vibration, Auburn, USA*, pp. 779–786. AL: Int. Science Publications.

Newland, D. E. & Hunt, H. E. M. 1996 The effect of variable foundation properties on railway-track vibration. *Proc. 4th Int. Congress on Sound and Vibration, St. Petersburg, Russia*, vol. 2, pp. 1065–1072. AL: Int. Science Publications.

Schofield, A. N. 1980 Cambridge geotechnical centrifuge operations. *Geotechnique* **25**, 743–761.

Schofield, A. N. & Steedman, R. S. 1988 Recent development of dynamic model testing in geotechnical engineering. *Proc. 9th World Conf. on Earthquake Engineering, Japan Association for Earthquake Disaster Prevention, Kyoto–Tokyo*, vol. 8, pp. 813–824.

Skudrzyk, E. 1971 *The foundations of acoustics*. Springer.

Tait, C. & Findlay, W. 1996 Wavelet analysis for onset detection. *Proc. Int. Computer Music Conf., ICMA, Hong Kong*, pp. 500–503.

Taylor, R. N. (ed.) 1995 *Geotechnical centrifuge technology*. London: Blackie Academic & Professional and Chapman & Hall.

PHILOSOPHICAL TRANSACTIONS OF THE ROYAL SOCIETY A MATHEMATICAL, PHYSICAL & ENGINEERING SCIENCES

PHILOSOPHICAL TRANSACTIONS OF THE ROYAL SOCIETY A MATHEMATICAL, PHYSICAL & ENGINEERING SCIENCES

PHILOSOPHICAL TRANSACTIONS OF THE ROYAL SOCIETY A MATHEMATICAL, PHYSICAL & ENGINEERING SCIENCES

PHILOSOPHICAL TRANSACTIONS OF THE ROYAL SOCIETY A MATHEMATICAL, PHYSICAL & ENGINEERING SCIENCES

PHILOSOPHICAL TRANSACTIONS OF THE ROYAL SOCIETY A MATHEMATICAL, PHYSICAL & ENGINEERING SCIENCES

PHILOSOPHICAL TRANSACTIONS OF THE ROYAL SOCIETY A MATHEMATICAL, PHYSICAL & ENGINEERING SCIENCES